Estimating the surface layer refractive index structure constant over snow and sea ice using Monin-Obukhov similarity theory with a mesoscale atmospheric model

CHUN QING,[1,2] XIAOQING WU,[1] HONGHUA HUANG,[1] QIGUO TIAN,[3] WENYUE ZHU,[1] RUIZHONG RAO,[1] AND XUEBIN LI[1,*]

[1]*Key Laboratory of Atmospheric Composition and Optical Radiation, Anhui Institute of Optics and Fine Mechanics, Chinese Academy of Science, Hefei, Anhui 230031, China*
[2]*Science Island Branch of Graduate School, University of Science and Technology of China, Hefei, Anhui 230026, China*
[3]*Polar Research Institute of China, Shanghai 200136, China*
[*] xbli@aiofm.ac.cn

Abstract: Since systematic direct measurements of refractive index structure constant (C_n^2) for many climates and seasons are not available, an indirect approach is developed in which C_n^2 is estimated from the mesoscale atmospheric model outputs. In previous work, we have presented an approach that a state-of-the-art mesoscale atmospheric model called Weather Research and Forecasting (WRF) model coupled with Monin-Obukhov similarity (MOS) theory which can be used to estimate surface layer C_n^2 over the ocean. Here this paper is focused on surface layer C_n^2 over snow and sea ice, which is the extending of estimating surface layer C_n^2 utilizing WRF model for ground-based optical application requirements. This powerful approach is validated against the corresponding 9-day C_n^2 data from a field campaign of the 30th Chinese National Antarctic Research Expedition (CHINARE). We employ several statistical operators to assess how this approach performs. Besides, we present an independent analysis of this approach performance using the contingency tables. Such a method permits us to provide supplementary key information with respect to statistical operators. These methods make our analysis more robust and permit us to confirm the excellent performances of this approach. The reasonably good agreement in trend and magnitude is found between estimated values and measurements overall, and the estimated C_n^2 values are even better than the ones obtained by this approach over the ocean surface layer. The encouraging performance of this approach has a concrete practical implementation of ground-based optical applications over snow and sea ice.

References and links

1. V. I. Tatarskii, *Wave Propagation in a Turbulent Medium* (McGraw-Hill, 1961).
2. J. S. Lawrence, M. C. B. Ashley, A. Tokovinin, and T. Travouillon, "Exceptional astronomical seeing conditions above Dome C in Antarctica," Nature **431**(7006), 278-281 (2004).
3. E. Masciadri, J. Vernin, and P. Bougeault, "3D numerical simulations of optical turbulence at the Roque de Los Muchachos Observatory using the atmospherical model Meso-Nh," A&A. **365**, 699-708 (2001).
4. E. Masciadri, "Near ground wind simulations by a meso-scale atmospherical model for the extremely large telescopes site selection," Rev. Mex. Astron. Astrofis. **39**, 249-259 (2003).
5. E. Masciadri and F. Lascaux, "MOSE: a feasibility study for optical turbulence forecasts with the Meso-Nh mesoscale model to support AO facilities at ESO sites (Paranal and Armazones)," Proc. SPIE **8447**, 84475A (2012).
6. F. Lascaux, E. Masciadri, and L. Fini, "MOSE: operational forecast of the optical turbulence and atmospheric parameters at European Southern Observatory ground-based sites - II. Atmospheric parameters in the surface layer 0-30 m," MNRAS **436**, 3147-3166 (2013).
7. F. Lascaux, E. Masciadri and L. Fini, "Forecast of surface layer meteorological parameters at Cerro Paranal with a mesoscale atmospherical model," MNRAS. **449**, 1664-1678 (2015).

8. S. Cheinet, A. Beljaars, K. Weiss-Wrana and Y. Hurt, "The use of weather forecasts to characterise near-surface optical turbulence," Boundary-Layer Meteor. **138**, 453-473 (2011).
9. J. C. Wyngaard, *On surface-layer turbulence* (American Meteorological Society, Boston, Mass., 1973).
10. M. L. Wesely and E. C. Alcaraz, "Diurnal cycles of the refractive index structure function coefficient," J. Geophys. Res. **78**(27), 6224-6232 (1973).
11. K. L. Davidson, G. E.Schacher, C. W. Fairall and A. K. Goroch, "Verification of the bulk method for calculating overwater optical turbulence," Appl. Opt. **20**(17), 2919-2924 (1981).
12. K. E. Kunkel and D. L. Walters, "Modeling the diurnal dependence of the optical refractive index structure parameter," J. Geophys. Res. **88**(C15), 10999-11004 (1983).
13. E. L. Andreas, "Estimating C_n^2 over snow and ice from meteorological data," J. Opt. Soc. Am. A **5**(4), 481-495 (1988).
14. D. L. Hutt, "Modeling and measurements of atmospheric optical turbulence over land," Opt. Eng. **38**(8), 1288-1295 (1999).
15. P. A. Frederickson, K. L. Davidson, C. R. Zeisse, and C. S. Bendall, "Estimating the refractive index structure parameters (C_n^2) over the ocean using bulk methods," J. Appl. Meteorol. **39**, 1770-1783 (2000).
16. A. Tunick, "C_n^2 model to calculate the micrometeorological influences on the refractive index structure parameter," Environ. Model. Softw. **18**, 165-171 (2003).
17. V. P. Lukin, V. V. Nosov, O. N. Emaleev, and E. V. Nosov, "Semiempirical hypotheses of the turbulence theory in anisotropic boundary layer," Proc. SPIE **5743**, 110-130 (2004).
18. V. V. Nosov, V. P. Lukin, O. N. Emaleev, and E. V. Nosov, "Semiempirical hypotheses of the turbulence theory in the atmospheric anisotropic boundary layer (for mountain region)," Proc. conference "Vision for infrared astronomy," France, 155-160 (2006).
19. C. Qing, X. Wu, X. Li, W. Zhu. C. Qiao, R. Rao and H. Mei, "Use of weather research and forecasting model outputs to obtain near-surface refractive index structure constant over the ocean," Opt. Express **24**(12), 13303-13315 (2016).
20. D. S. Wilks, *Statistical Methods in the Atmospheric Sciences* (Academic Press, 1995).
21. J. E. Thornes and D. B. Stephenson, "How to judge the quality and value of weather forecast products," Meteorol. Appl. **8**, 307-314 (2001).
22. I. T. Jolliffe and D. B. Stephenson, *Forecast Verification. A Practitioner's Guide in Atmospheric Science* 2nd ed. (Wiley, 2003).
23. X. Wu, Q. Tian, P. Jiang, B. Chai, C. Qing, J. Cai, X. Jin, and H. Zhou, "A new method of measuring optical turbulence of atmospheric surface layer at Antarctic Taishan Station with ultrasonic anemometer," Adv. Polar. Sci. **26**(4), 305-310 (2015).
24. Q. Tian, P. Jiang, X. Wu, X. Jin, S. Lu, T. Ji, B.Chai, S. Zhang, and H. Zhou, "A mobile polar atmospheric parameter measurement system: II. First atmospheric turbulence observation at Antarctic Taishan Station," Adv. Polar. Sci. **26**(2), 140-146 (2015).
25. C. E. Coulman, "A quantitative treatment of solar 'seeing' I ", Solar Physics. **7**, 122-143 (1969).
26. R. D. Marks, J. Vernin, M. Azouit, J. W. Briggs, M. G. Burton, M. C. B. Ashley, and J. F. Manigault, "Antarctic site testing-microthermal measurements of surface-layer seeing at the South Pole," Astronomy Astrophys. **118**, 385-390 (1996).
27. W. G. Large and S. Pond, "Sensible and latent heat flux measurements over the ocean," J. Phys. Oceanogr. **12**, 464-482 (1982).
28. C. A.Paulson, "The mathematical representation of wind speed and temperature profiles in the unstable surface layer," J. Appl. Meteorol. **9**, 857-861 (1970).
29. C. W. Fairall, E. F. Bradley, D. P. Rogers, J. B. Edson, and G. S. Young, "Bulk parameterization of airsea fluxes for tropical oceanglobal atmosphere coupledocean atmosphere response experiment," J. Geophys. Res. **101**(C2), 3747-3764 (1996).
30. L. Mahrt, "Stratified atmospheric boundary layers," Boundary-Layer Meteor **90**, 375-396 (1999).
31. J. B. Edson, C. W. Fairall, P. G. Mestayer, and S. E. Larsen, "A study of the inertial-dissipation method for computing air-sea fluxes," J. Geophys. Res. **96**, 10689-10711 (1991).

1. Introduction

Atmospheric turbulence is the major reason for serious decline of imaging quality of the ground-based optical applications (e.g., astronomical observation, laser communication and target detection). The intensity of atmospheric turbulence is usually described by refractive index structure constant, C_n^2 ($m^{-2/3}$) [1]. Antarctic Plateau has become a potential great interest of astronomical site, as its extremely low temperature, dryness, typical high altitude, and joint to the fact that the optical turbulence seems to be concentrated in a thin surface layer (e.g., [2]). However, systematic direct measurements of C_n^2 for many climates and seasons are not available, especially in severe environment, and it varies considerably from location to location. In many

cases, it is impractical and expensive to deploy instrumentation to characterize the atmospheric turbulence, making simulations a less expensive and convenient alternative. Over the years, only a handful of studies documented the characteristics of surface layer atmospheric parameters with a Mesoscale Non-hydrostatic (Meso-Nh) model above the sites of interest for astronomy: at Roque de los Muchachos (surface layer temperature, [3]); MOSE (Modelling ESO Sites) project that aims to prove the feasibility of the forecast of the atmospheric parameters above the two European Southern Observatory (ESO) ground-based sites Cerro Paranal in Chile and Maidanak in Uzbekistan (surface layer wind speed, [4-7]). An extended review of alternative methods for calculating surface layer C_n^2 using European Center for Medium Range Weather Forecasts (ECMWF) model products over climatologically distinct sites in western Europe can be found in Cheinet's paper [8], and this method forecast some essential aspects of surface layer C_n^2. Even though there is considerable diversity among the reported results, quasi-universality of the simulated surface layer C_n^2 with a mesoscale model is not clearly discernible. Each existing approach has its own merits and limitations, but none of them is known to be superior.

MOS theory provides a rigorous scientific basis to estimate C_n^2 from routine meteorological parameters in the surface layer (refer to [9-18] and the references therein). In previous work, we have presented an alternative approach that WRF model coupled with MOS theory which can be used to estimate C_n^2 over the ocean surface layer [19]. On account of the various ground-based optical application requirements, the purpose of this paper is to present a marked result of estimating surface layer C_n^2 over snow and snow-covered sea ice with a atmospheric model and expand on the analyses in several ways. In this study, we have analysed the performance of this approach in reconstructing surface layer C_n^2 over snow and sea ice by comparing estimated values with the corresponding C_n^2 data from a field campaign of the 30th CHINARE, in January 2014.

We have analysed the results of the bias, root mean square error (RMSE), bias-corrected RMSE (σ) and correlation coefficient (R_{xy}) between estimated values and in-situ measurements of C_n^2. It is worth noting that in spite of being fundamental statistical operators and providing key information to evaluate the model simulation, the bias, RMSE, σ and R_{xy} do not provide the necessary information we would like to have in terms of this approach performance. To investigate the quality of model estimation, a method widely used in the atmosphere physics, as well as other fields such as economy and medicine, consists of constructing and analysing contingency tables [20-22]. From these tables, it is possible to derive a number of different parameters that describe the quality of this approach performance. A contingency table allows for analysis of the relationship between two or more categorical variables. From the temporal evolution, correlation and cumulative distributions and contingency tables for values estimated and in-situ measurement, the results are very encouraging and remarkable. This approach may be applied to the ground-based optical applications over snow and sea ice.

In Section 2, we present the in-situ measurement system and model configuration. In Section 3, the theoretical basis is described. In Section 4, the temporal evolution of C_n^2 for estimation and in-situ measurement are presented, together with the statistical analysis used in the study. In Section 5, we discuss the uncertainties and the possible improvement room for this approach. Finally, conclusions are drawn in Section 6.

2. Measurement system and WRF model configuration

2.1. In-situ measurement system and the principle of micro-thermometer

Antarctic Taishan Station (76°58′E, 73°51′S, altitude 2621 m) is located in Princess Elizabeth Land between Chinese Antarctic Zhongshan and Kunlun stations. In 2013, a mobile atmospheric parameter measurement system was designed and constructed to measure C_n^2 and meteorological parameters in Antarctic Taishan Station [23, 24], which is close to the center grid point (76°58′E, 73°51′S) of simulation domain. The Antarctic Taishan Station mo-

bile atmospheric parameter measurement system includes a data collector (CR5000), ultrasonic anemometer (CSAT3), micro-thermometer, temperature and humidity probe (HMP155), wind monitor (05103V), barometer (CS106), communication module, power module and a 3-meter tower, which is shown in Fig. 1. Two levels (0.5 m and 2 m above ground) of air temperature, relative humidity, wind speed and one level (2 m) of air pressure and atmospheric turbulence intensity can be measured at the same time. We observed C_n^2 in the surface layer for the first time at Antarctic Taishan Station using the micro-thermometer and three-dimensional ultrasonic anemometer simultaneously from 30 December 2013 to 10 February 2014 in the 30th CHINARE. This paper presents our part results from 11 January to 19 January in 2014. C_n^2 values measured by micro-thermometer are used to validate C_n^2 values simulated by this approach.

Fig. 1. Mobile atmospheric parameter measurement system over snow and sea ice at Antarctic Taishan Station.

The refractive index structure constant C_n^2 is connected with the temperature structure constant C_T^2 of the micro-thermometer field variations which mainly produce fluctuations in the refractive index at optical wavelengths [25, 26]. The relationship between C_n^2 and C_T^2 is given as follow:

$$C_n^2 = (79 \times 10^{-6} \frac{P}{T^2})^2 C_T^2, \tag{1}$$

where T is air temperature (K), and P is air pressure (hPa). The C_T^2 is defined as the constant of proportionality in the inertial subrange form of the temperature structure function $D_T(r)$. The process for calculating C_T^2 involves the measurement of the square and average of the temperature difference given by two probes which are separated by a known distance r in the inertial region. For a Kolmogorov type spectrum, C_T^2 is related to the temperature structure function $D_T(r)$ as below:

$$D_T(r) = \langle [T(\vec{x}) - T(\vec{x} + \vec{r})]^2 \rangle$$
$$= C_T^2 r^{2/3} \ for \ l_0 \ll r \ll L_0 . \tag{2}$$

where $\vec{x}$ and $\vec{r}$ denote the position vector, r is the magnitude of $\vec{r}$, $\langle ... \rangle$ represents the ensemble average, l_0 and L_0 are the inner and outer scales of the atmospheric turbulence respectively

and have units of m. In this study, a 10 μm diameter, 20 mm long platinum wire is used as micro-thermometer probe, and the equivalent noise is about 0.002 K (see [19] in detail). The platinum probe has a linear resistance-temperature coefficient, and responds to an increase in atmospheric temperature with an increase in resistance. In our case, the probes are used to measure the temperature difference at two points which are horizontally separated by 1.0 m apart. The two probes are legs of a Wheatstone bridge, and the resistance of the probe is very nearly proportional to temperature, thus temperature changes are sensed as an imbalance voltage of the bridge. The micro-thermometer system provides C_T^2 data by measuring mean square temperature fluctuations and then C_n^2 data can be acquired.

2.2. WRF model configuration and sample selection

WRF model is a mesoscale atmospheric model used for both professional forecasting and atmospheric research, developed jointly between the National Center for Atmospheric Research (NCAR) and the National Oceanic and Atmospheric Administration (NOAA) of the United States. The model is based on the Navier-Stokes equations which are solved numerically on a three dimensional grid. The model simulates four basic atmospheric properties: wind, pressure, temperature and atmospheric water vapor. All other variables are derived from these four parameters. Details of governing equations, transformations and grid adaptation are given in the Modeling System User's Guide. In this study, WRF model is initialized with the Final Operational Global Analysis (FNL) data which has a horizontal resolution of $1° \times 1°$ (in longitude and latitude), downloaded from the web site of National Center of Environment Prediction (NCEP). The Antarctic plateau map is shown in Fig. 2.
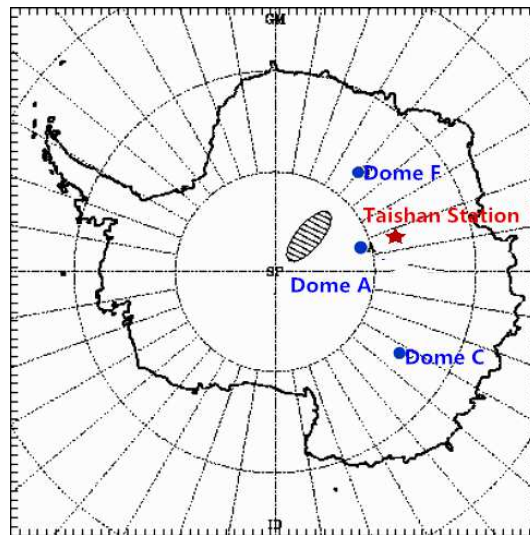

Fig. 2. Antarctic Plateau map. The site of mobile atmospheric parameter measurement system is noted with a red solid star. The blue solid circles represent the Dome A, Dome C and Dome F, respectively.

A triple-nested numerical modeling domain, of which the nesting ratio is 5, with the coarse horizontal resolution of 12.5 km and grid points of 90, as well as the finest horizontal resolution of 0.5 km and grid points of 45, is used in this study. The basic parameter settings are listed in Table 1.

WRF model exports a large number of meteorological parameters (pressure, temperature, absolute humidity, wind speed, etc.), which depend upon the physical schemes that have been

Table 1. The basic parameter settings. ΔX represents the grid horizontal resolution.

Basic parameter	Settings
Center longitude and latitude	76°58′E, 73°51′S
ΔX, Number of grid points (Domain 1)	12.5 km, 90 × 90
ΔX, Number of grid points (Domain 2)	2.5 km, 75 × 75
ΔX, Number of grid points (Domain 3)	0.5 km, 45 × 45
Initialized field data	FNL
Vertical layers	40
Output time interval	10 minutes

chosen for the simulation. Other numerical details are omitted here for brevity, and interested readers are encouraged to peruse WRF User's Guide to gain a better understanding of mesoscale modeling. The main physical scheme settings are listed in Table 2.

Table 2. The main physical scheme settings.

Main physical scheme	Settings
Micro-physics process	WSM-5
Longwave radiation	RRTM
Shortwave radiation	Goddard
Boundary layer	Eta similarity
Ground process	Noah
Planetary boundary layer	MYJ
Cumulus parameterization	Kain-Fritsch

To validate the performance of this approach, a set of 9 different nights C_n^2 data measured by micro-thermometer from a part of field campaign of the 30th CHINARE are sampled, since WRF model each run is time-consuming and costs huge computational resource. Besides, WRF model is run on 3 different nights (starting at Jan 10, 13, 16, respectively) using the procedure described before, and all the simulation times are listed in Table 3. We should note that the measurement system exports C_n^2 values at 5 seconds interval, while WRF model outputs results at 10 minutes interval owing to the model configuration limitation. The measured values are averaged over the same interval (10 minutes) to match with the simulated ones for a meaningful comparison. We also note that WRF model outputs are saved as UTC time format while the micro-thermometer values are saved as Local time format, and the conversion between them is Local time = UTC time + 05:00.

Table 3. Simulation times.

Simulation No.	Simulation time	
	Start time	End time
1	2014-01-10-19:00 UTC	2014-01-13-19:00 UTC
2	2014-01-13-19:00 UTC	2014-01-16-19:00 UTC
3	2014-01-16-19:00 UTC	2014-01-19-19:00 UTC

3. Theoretical basis

For estimation of surface layer C_n^2 we chose the following semiempirical model, which is based on the MOS theory. From visible to near-infrared wavelengths, a wide range of physically-based

approach for the estimation of C_n^2 exists in the literature (see [13] for details). The expression C_n^2 can be defined in terms of C_T^2, C_q^2 and C_{Tq} as follows :

$$C_n^2 = A^2 C_T^2 + 2ABC_{Tq} + B^2 C_q^2. \tag{3}$$

where the coefficient A and B are related to the wavelength (μm), pressure (hPa) and temperature (K). At a interest wavelength of 0.55 μm, A = $79.0 \times 10^{-6} \frac{P}{T^2}$ and B = -56.4×10^{-6}. C_T^2, C_q^2 and C_{Tq} are the temperature structure parameter, humidity structure parameter and temperature-humidity structure parameter, respectively. Once C_T^2, C_q^2 and C_{Tq} are estimated, it is relatively straightforward to estimate C_n^2.

The dimensionless function (ξ) is used to express the surface layer atmospheric dynamic property, defined as:

$$\xi = \frac{z k g (T_* + 0.61 T q_*)}{\vartheta_v u_*^2}. \tag{4}$$

in which z (m) is the height above the surface, k is the von-Karman constant (0.4), g (ms^{-2}) is the gravitational acceleration, ϑ_v (K) is the virtual potential temperature, T_*, q_* and u_* are the scaling parameters for temperature, absolute humidity and wind speed, respectively.

By using MOS theory in atmospheric surface layer, the expressions C_T^2, C_q^2 and C_{Tq} can be expressed in terms of T_* and q_* as follows:

$$C_T^2 = T_*^2 z^{-2/3} f_T(\xi), \tag{5a}$$

$$C_q^2 = q_*^2 z^{-2/3} f_q(\xi), \tag{5b}$$

$$C_{Tq} = \gamma_{Tq} T_* q_* z^{-2/3} f_{Tq}(\xi). \tag{5c}$$

where γ_{Tq} is the temperature-humidity correlation coefficient. We use a value of 0.5 for γ_{Tq} when $\frac{\Delta T}{\Delta q} \leq 0$, and a value of 0.8 when $\frac{\Delta T}{\Delta q} \geq 0$ in this work, following [15]. The similarity functions $f_T(\xi)$, $f_q(\xi)$ and $f_{Tq}(\xi)$ are determined by experiment, and supposed to $f_T(\xi) = f_q(\xi) = f_{Tq}(\xi)$ usually [13]. The similarity function $f(\xi)$ is given by Wyngaard [9] during a field campaign in Kansas:

$$f(\xi) = \begin{cases} 4.9(1 - 7\xi)^{-2/3}, & \xi \leq 0, \\ 4.9(1 + 2.75\xi), & \xi \geq 0. \end{cases} \tag{6}$$

Subsequently, substituting Eqs. (5-6) into Eq. (3) gives a C_n^2 expression in terms of the T_* and q_*:

$$C_n^2 = z^{-2/3} f(\xi)(A^2 T_*^2 + 2AB\gamma_{Tq} T_* q_* + B^2 q_*^2). \tag{7}$$

According to MOS theory, the average vertical profiles of wind speed $U(z)$, temperature $T(z)$ and absolute humidity $q(z)$ within the surface layer are defined as follows:

$$\frac{\partial U(z)}{\partial z} = \frac{u_*}{kz} \varphi_m(\xi), \tag{8a}$$

$$\frac{\partial T(z)}{\partial z} = \frac{T_*}{kz} \varphi_h(\xi), \tag{8b}$$

$$\frac{\partial q(z)}{\partial z} = \frac{q_*}{kz} \varphi_q(\xi), \tag{8c}$$

where the functions $\varphi_m(\xi)$, $\varphi_h(\xi)$ and $\varphi_q(\xi)$ must be found experimentally. Although there is

no consensus yet on their forms, the measurements seem to be converging toward the functions used by Large and Pond [27]. For unstable conditions ($\xi \leq 0$)

$$\varphi_m(\xi) = (1 - 16\xi)^{-1/4}, \tag{9a}$$

$$\varphi_h(\xi) = \varphi_q(\xi) = (1 - 16\xi)^{-1/2}. \tag{9b}$$

For stable conditions ($\xi \geq 0$)

$$\varphi_m(\xi) = \varphi_h(\xi) = \varphi_q(\xi) = 1 + 7\xi. \tag{10}$$

Paulson [28] showed how to integrate Eq. (8) with the empirical functions Eqs. (9)-(10). The scaling parameters u_*, T_* and q_* within atmospheric surface layer are given by Eq. (11)

$$u_* = kU(z)[ln(\frac{z}{z_{oU}}) - \Phi_m(\xi)]^{-1}, \tag{11a}$$

$$T_* = k[T(z) - T_s][ln(\frac{z}{z_{oT}}) - \Phi_h(\xi)]^{-1}, \tag{11b}$$

$$q_* = k[q(z) - q_s][ln(\frac{z}{z_{oq}}) - \Phi_h(\xi)]^{-1}, \tag{11c}$$

where T_s and q_s are the surface temperature and surface absolute humidity, respectively. z_{oU}, z_{oT} and z_{oq} are the "roughness lengths" of wind speed, temperature and absolute humidity respectively, which can be parameterized by routine meteorological parameters as well (see [29] for details). The functions $\Phi_m(\xi)$ and $\Phi_h(\xi)$ are the integrated forms of the functions $\varphi_m(\xi)$ and $\varphi_h(\xi)$, respectively. For unstable conditions ($\xi \leq 0$)

$$\Phi_m(\xi) = 2ln[\frac{1 + x}{2}] + ln[\frac{1 + x^2}{2}] - arctan(x) + \frac{\pi}{2}, \tag{12a}$$

$$\Phi_h(\xi) = 2ln[\frac{1 + x^2}{2}]. \tag{12b}$$

where $x = (1 - 16\xi)^{1/4}$. For stable conditions ($\xi \geq 0$)

$$\Phi_m(\xi) = \Phi_h(\xi) = -7\xi. \tag{13}$$

Thus, with estimated values of the $U(z)$, $T(z)$ and $q(z)$, as well as the T_s and q_s, we can obtain u_*, T_*, q_* and ξ by solving Eq. (4) and Eqs. (11)-(13) iteratively (see [13, 19] for details). Finally, with these values of u_*, T_*, q_* and ξ, it is simple to estimate C_n^2 from Eq. (7).

4. Results

4.1. Temporal evolution of C_n^2 for model and measurement

Figure 3 compares the temporal evolution of surface layer C_n^2 over snow and sea ice between model and measurement. One can see that estimated C_n^2 agrees reasonably well with that measured by micro-thermometer in trend and magnitude in general. This approach qualitatively captures several "sharp drop-offs" of C_n^2 during morning and evening transitions in a faithful manner which are clearly visible in this plot. In some cases, these "sharp drop-offs" are estimated earlier by about one hour. Moreover, some specific feature C_n^2 for snow and ice surface layer has been displayed in Fig. 3 where the diurnal variation of the estimated C_n^2 and the measured C_n^2 are all obvious and the peak value of C_n^2 is not the most strong at noontime, while strong at night, especially the time from nightfall to midnight.

Quite interestingly, estimated C_n^2 values tend to be overestimated slightly from nightfall to midnight, while having a relatively better performance in the low range of C_n^2. The surface heterogeneity has a much greater impact on atmospheric turbulence in stable conditions [30], and the categories of snow and sea ice are more homogeneous than that of underlying surface relatively. In this study, the simulation area is in an open snow and sea ice surface where the atmospheric turbulence is impacted by the surroundings slightly. While in that study over the coastal ocean surface layer, the atmospheric turbulence is impacted by the surroundings greatly and MOS theory will be invalid if the dynamic atmospheric properties depend upon surface characteristics excessively. Thus, it is fair to expect that the C_n^2 values obtained by this approach over snow and sea ice surface layer are better than the ones obtained over the ocean surface layer [19].
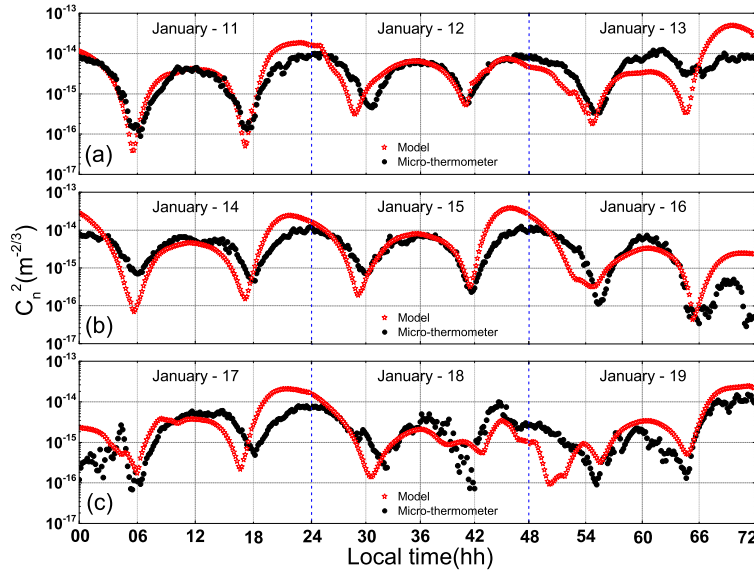

Fig. 3. Temporal evolution of the surface layer C_n^2 (about 2 m) over snow and sea ice during January 11 to 19, 2014 (panels a-c depict simulations No.1-3, respectively). The red open star and the black dots represent the model and micro-thermometer, respectively.

4.2. The correlation and cumulative distributions

We evaluate the reliability of C_n^2 estimated by this approach using four statistical operators: the bias, the root mean square error (RMSE), the bias-corrected RMSE (σ) and the correlation coefficient (R_{xy}). The expression bias, RMSE, R_{xy} are defined as:

$$bias = \sum_{i=0}^{N} \frac{\Delta_i}{N}, \tag{14a}$$

$$RMSE = \sqrt{\sum_{i=0}^{N} \frac{(\Delta_i)^2}{N}}, \tag{14b}$$

$$R_{xy} = \frac{\sum_{i=0}^{N}(X_i - \overline{X}_i)(Y_i - \overline{Y}_i)}{\sqrt{\sum_{i=0}^{N}(X_i - \overline{X}_i)^2 \sum_{i=0}^{N}(Y_i - \overline{Y}_i)^2}}, \tag{14c}$$

with $\Delta_i = Y_i - X_i$, where X_i is the individual C_n^2 value measured by the micro-thermometer, Y_i the individual C_n^2 value estimated by this approach at the same time and N is the number of times for which a couple (X_i, Y_i) is available. $\overline{X}_i$ and $\overline{Y}_i$ represent the average value of measured and estimated parameters. From the bias and the RMSE, we deduce the bias-corrected rmse (σ):

$$\sigma = \sqrt{RMSE^2 - bias^2}. \qquad (15)$$

The correlation of $\log_{10}(C_n^2)$ between model and measurement is depicted in Fig. 4(a), and the values of bias, RMSE, σ and R_{xy} are noted in the left-top of Fig. 4(a). We can see that the values of bias, RMSE and σ are very small and the data scatter is rather small, while the R_{xy} is high relatively, which shows again the estimated values are coherent with the measurements well. There's one point which needs attention that the estimated values have relatively large drift compared with in-situ measurements when $\log_{10}(C_n^2)$ is greater than -14.25.
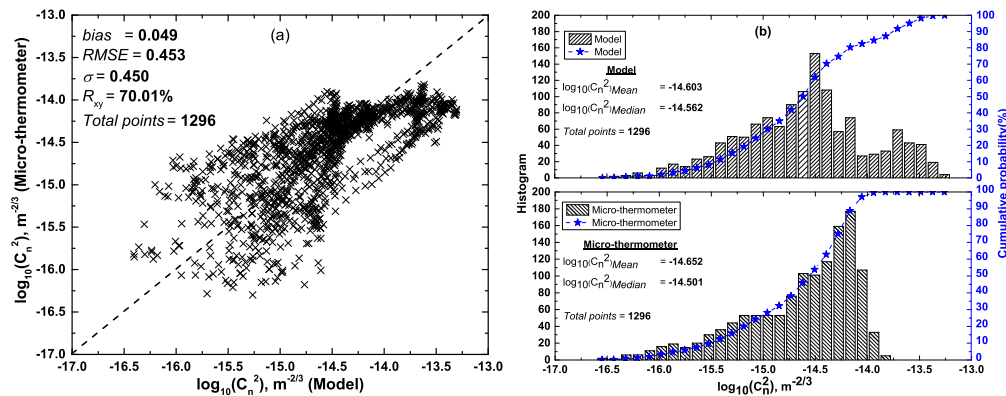

Fig. 4. Statistical analysis of the surface layer C_n^2 over snow and sea ice for model and micro-thermometer. (a) The correlation between model (abscissa) and micro-thermometer (ordinate); (b) The histograms (black histogram, left scale) and cumulative distributions (blue symbol curves, right scale) of $\log_{10}(C_n^2)$, the top and bottom panels for model and micro-thermometer, respectively.

The histograms and cumulative distributions for $\log_{10}(C_n^2)$ are shown in Fig. 4(b). Estimated values are coherent with measured values in a large probability distribution ($\geq$ 80%), while the estimated values distribute in a relatively wide C_n^2 range, which is to say that estimated values relatively are larger than measurements when $\log_{10}(C_n^2)$ is greater than -14.25. From the cumulative distributions, we can extract the mean (-14.603 versus -14.652) and the median (-14.562 versus -14.501) of $\log_{10}(C_n^2)$ for values estimated and measurements, which are close to each other (noted in the left-middle of the top and bottom panels in Fig. 4(b)). Consequently, we confirm that the estimated values in this approach are reliable overall.

4.3. Contingency table

As mentioned in the introduction, we utilize a contingency table to investigate the relationship between estimated values and measurements. A contingency table allows for analysis of the relationship between two or more categorical variables, which is a table with $n \times n$ entries that displays the distribution of model and measurement in terms of frequencies or relative frequencies. For our purpose, a 2×2 table, however, is too simple to analyze this model. A 3×3 table is definitely more appropriated. It consists of the dividing estimated and measured

values in some categories delimited by some thresholds. An example of a 3×3 contingency table is shown in Table 4.

Table 4. Generic 3×3 contingency table.

| Intervals | | Measurement | | |
	interval 1	interval 2	interval 3	total
interval 1	a (hit 1)	b	c (miss)	a + b + c
interval 2	d	e (hit 2)	f	d + e + f
interval 3	g (miss)	h	i (hit 3)	g + h + i
total	a + d + g	b + e + h	c + f + i	N = a + b + c + d + e + f + g + h + i

(Model on left side, spanning interval rows)

There are two cases where the "hit" represents that the estimated value is correct, and the "miss" represents that the estimated value is incorrect [21]. Using a, b, c, d, e, f, g, h, i and N ($N = a + b + c + d + e + f + g + h + i$), we can compute different probabilities useful to have an insight on how well (or bad) this approach performs for a particular parameter. With all the different simple scores (a, b, c, d, e, f, g, h, i) listed, we will use them in the following of the paper from the generic 3×3 contingency table of Table 4. The percent of correct detections (PC, in %), probability of detection (POD, in %) and extremely bad detection (EBD, in %) are given below

$$PC = \frac{a + e + i}{N} \times 100, \ 0\% \leq PC \leq 100\%, \tag{16a}$$

$$POD(event\ 1) = \frac{a}{a + d + g} \times 100, \ 0\% \leq POD \leq 100\%, \tag{16b}$$

$$POD(event\ 2) = \frac{e}{b + e + h} \times 100, \ 0\% \leq POD \leq 100\%, \tag{16c}$$

$$POD(event\ 3) = \frac{i}{c + f + i} \times 100, \ 0\% \leq POD \leq 100\%, \tag{16d}$$

$$EBD = \frac{c + g}{N} \times 100, \ 0\% \leq EBD \leq 100\%. \tag{16e}$$

where PC =100% is the best score and corresponds to a perfect estimation. POD =100% is the best score, which represents the proportion of measured values that have been correctly estimated by this approach. EBD represents the percent of the most distant estimated values by this approach from the measurements, and it is equal to 0% for a perfect estimation. In the case of a perfectly random estimation ($a = b = ... = i = \frac{N}{9}$), all POD are equal to 33%, PC=33% and EBD=22.2%. The model is useful if these values perform better than those random cases (33% or 22.2%). These values are a good reference to evaluate the performances of this approach. We will write POD_i instead of POD ($event\ i$) with the i event considered (seen in Eq. (16)).

Here, the variables we considered are the measurement of C_n^2, and the corresponding C_n^2 estimated by this approach. As seen in Table 5, we can observe that the PC (63.66%) is significatively better than 33% (value of random case). Moreover, the EBD (1.77%) is well smaller than 22.2% and even negligible, which is the sign that this approach never produces extremely bad estimation. POD_1 (event 1) is 72.18%, POD_2 (event 2) is 50.66% and POD_3 (event 3) is 66.40%. In all cases, PC and $POD_{i=1,2,3}$ are well larger than 33% (value of random case). This proves therefore the utility of this approach.

Table 5. A 3×3 contingency table for $\log_{10}(C_n^2)$ between model (row) and micro-thermometer (column)[a]. Interval 1 represents $\log_{10}(C_n^2) \leq$ -14.803, interval 2 represents -14.803 $\leq \log_{10}(C_n^2) \leq$ -14.348, interval 3 represents $\log_{10}(C_n^2) \geq$ -14.348. This two thresholds (-14.803 and -14.348) are defined with the climatological tertiles [6].

	Intervals	Measurement			
		interval 1	interval 2	interval 3	total
Model	interval 1	301 (hit 1)	131	14 (miss)	446
	interval 2	107	192 (hit 2)	154	453
	interval 3	9 (miss)	56	332 (hit 3)	397
	total	417	379	500	N = 1296

[a]PC = 63.66%; EBD = 1.77%; POD_1 = 72.18%; POD_2 = 50.66%; POD_3 = 66.40%

5. Discussion

Although the estimated C_n^2 agrees with the measured C_n^2 as a whole, there still exists some room for improvement. Here we discuss the uncertainties and the possible improvement for this approach.

Firstly, the C_n^2 value measured by micro-thermometer could be considered as the "point" measurement at a limited domain, while the estimated C_n^2 should be considered as the 10 minutes statistical average value which is a simple process of various influencing factor to atmospheric turbulence at 0.25 km^2 area for the center of simulation domain. In future work, improvements are expected from WRF model finer horizontal grid resolution as well as the outputs time interval.

Secondly, the form of the similarity function $f(\xi)$ and empirical function $\varphi(\xi)$ is very important to the accuracy of estimating C_n^2 [31]. The conclusive and justify form of $f(\xi)$ and $\varphi(\xi)$ is determined difficultly. Nevertheless, the structure is similar and the coefficient is just only different. Hence, choosing a quite appropriate form of $f(\xi)$ and $\varphi(\xi)$ will improve the accuracy. The form of $f(\xi)$ cited in this paper is determined in the Kansas experiment in 1968 [9], and also cited in the Andreas's paper to estimate C_n^2 over snow and sea ice [13]. We will do more sufficient field experiments to gain a more quite appropriate form of $f(\xi)$ and $\varphi(\xi)$ in following work.

Finally, the atmospheric turbulence is impacted by the surroundings slightly over open snow and sea ice surface layer in this study, but there still exist some uncertainties. The measurement height or the height where C_n^2 value was estimated with this approach may be above the constant flux layer in a region where MOS theory is invalid when the snow and sea ice surface layer can become very thin in very stable conditions [30]. In the future, we will do more sufficient field experiments to gain a more precise understanding for the performance of this approach under very stable conditions.

6. Conclusions

The performance of WRF model coupled with MOS theory in reconstructing the temporal evolution of surface layer C_n^2 over snow and sea ice has been investigated with the associated statistical operators and the contingency table. The reasonably good agreement in trend and magnitude is found between estimated values and measurements overall. For the associated statistical operators, the values of bias (0.049), RMSE (0.453) and σ (0.450) are very small, while the R_{xy} (70.01%) is high relatively, as well as the mean (-14.603 versus -14.652) and the

median (-14.562 versus -14.501) of $\log_{10}(C_n^2)$ between estimated values and measurements are close to each other. For the contingency table, the percent of correct detection (PC=63.66%) and extremely bad detection (EBD=1.77%) computed from 3×3 contingency tables are excellent. POD_i ($POD_1 = 72.18\%$; $POD_2 = 50.66\%$; $POD_3 = 66.40\%$) are all greater than 33% (a typical value for a random distribution). These results permit us to confirm the excellent performances of this approach, and even better than recent results obtained by this approach over the ocean surface layer. Thus, it is conceivable that this approach has a conservative ability to capture realistic temporal variations of surface layer C_n^2 over snow and sea ice. To be certain, more validation studies are needed.

We have concluded that the performance of this approach in reconstructing the temporal evolution of surface layer C_n^2 over snow and sea ice is satisfactory, and it is applicable to the ground-based optical applications over snow and sea ice.